Manuscript prepared for Atmos. Chem. Phys.
with version 3.2 of the LaTeX class copernicus.cls.
Date: 30 March 2012

Gas transport in firn: multiple-tracer characterisation and model intercomparison for NEEM, Northern Greenland - Supplementary Material

C. Buizert, P. Martinerie, V. V. Petrenko, J. P. Severinghaus, C. M. Trudinger, E. Witrant, J. L. Rosen, A. J. Orsi, M. Rubino, D. M. Etheridge, L. P. Steele, C. Hogan, J. C. Laube, W. T. Sturges, V. A. Levchenko, A. M. Smith, I. Levin, T. J. Conway, E. J. Dlugokencky, P. M. Lang, K. Kawamura, T. M. Jenk, J. W. C. White, T. Sowers, J. Schwander and T. Blunier

2 Methods

2.1 NEEM 2008 firn air campaign

The location of the North Greenland Eemian ice drilling project (NEEM) camp and the site of the 2008 firn air campaign are shown in Fig. 1. Drilling was performed alternatively in both holes with the Danish electromechanical shallow drill. The hole diameter is 103.6 mm. In order to have an undisturbed surface for the first sampling levels, the first 10 m were drilled with a hand auger producing the same diameter core and hole.

2.2 Physical characterisation of NEEM firn air site

Density data fitting was done by eye, and care was taken that the second derivative is continuous over the transitions between the stages. Surface density was chosen as $\rho = 0.35$ $\mathrm{g cm^{-3}}$. The density fit is given by

$$\begin{aligned} \rho &= a_1 + a_2 z + a_3 e^{a_4(16-z)} && \text{for } z < 16\mathrm{m} \\ \rho &= a_5 + a_6 z + a_7 z^2 && \text{for } 16 \le z < 110\mathrm{m} \\ \rho &= a_8 + a_9\left(1 - e^{a_{10}(z-110)}\right) && \text{for } z \ge 110\mathrm{m} \end{aligned} \quad (1)$$

The constants in Eq. (1) obtained in the fitting procedure can be found in Table 1.

2.3 Gas measurements

For SF_6, the IUP data (EU and US holes) have been rescaled by 0.9912 to place the data on the NOAA scale that we use in our atmospheric reconstructions (rescaling corresponds to a modern day offset of 0.06 ppt). After correcting the IUP data no inter-laboratory offsets were observed on either borehole.

For the US hole NOAA CH_4 data have been used exclusively where available (13 depth levels). For a remaining 5 depths we have no NOAA measurements, and for these depths we have used IUP data after scaling them in the following way to place them on the NOAA scale:

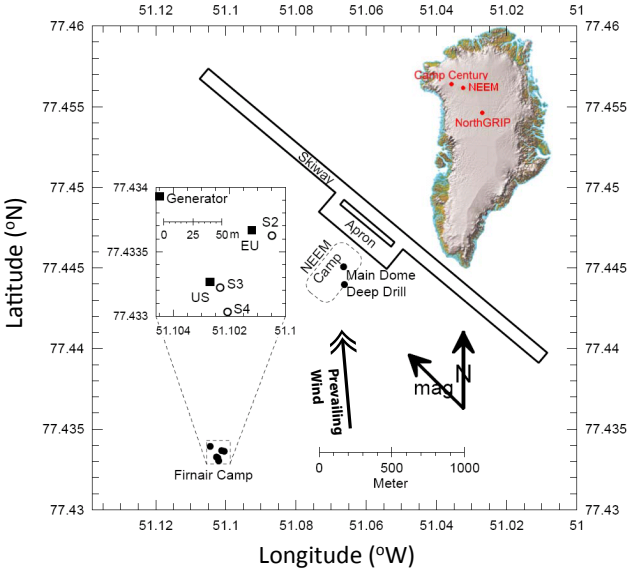

Fig. 1. Location of NEEM main structures and the site of the 2008 firn air campaign. The inset shows the position of the NEEM camp in Northern Greenland.

Table 1. Constants used in the density fitting Eq.(1).

Constant		
a_1	3.500000	$\times 10^{-1}$
a_2	1.359319	$\times 10^{-2}$
a_3	-1.569421	$\times 10^{-2}$
a_4	-4.300000	$\times 10^{-1}$
a_5	4.332293	$\times 10^{-1}$
a_6	7.976252	$\times 10^{-3}$
a_7	-3.536121	$\times 10^{-5}$
a_8	8.82746379	$\times 10^{-1}$
a_9	3.7853621	$\times 10^{-2}$
a_{10}	-5.198599	$\times 10^{-3}$

Table 2. Overview of radiocarbon measurements on NEEM firn air, expressed in $\Delta^{14}C$ notation. The replicate dev. gives the deviation of the replicate measurement from the first one.

Depth (m)	$\Delta^{14}C$ (‰)	ANSTO error (‰)	Replicate dev. (‰)	$[^{14}CO_2]$ ($\times 10^{-12}$ ppm)	Flask type
0.00	44.9	6.3	-	485.5	Glass
14.80	40.1	6.8	-	490.3	Glass
34.72	55.9	6.2	-	491.3	Glass
50.00	64.9	6.8	-	491.4	Glass
59.90	74.5	6.9	-	491.0	Glass
61.95	76.3	6.8	-	489.9	Glass
65.75	156.0	7.5	5.9	503.1	Glass
68.05	276.1	7.6	3.4	531.4	Glass, Stainless
70.05	349.0	6.3	-	546.5	Stainless
72.00	309.3	8.2	0.5	519.6	Glass, Stainless
74.08	165.4	7.3	-	455.8	Glass
75.90	45.1	7.2	4.8	407.4	Glass

$$[CH_4]_{NOAA} = 0.9933[CH_4]_{IUP} + 10.12 \quad (2)$$

This equation was obtained by correlating NOAA and IUP data on the US hole for depths where we have data from both labs (13 depths, R^2 =0.9995). The NOAA and CSIRO data on the EU borehole agree well and show no systematic offset.

Table 2 lists the radiocarbon measurements. CO_2 was extracted in May 2009 from 0.5 L glass sample flasks also used for CSIRO gas analysis, and in September 2009 the extracted CO_2 was graphitised at ANSTO. Measurements of $\Delta^{14}CO_2$ were performed on the ANTARES accelerator mass spectrometer. Since the sample collected at 70.05 m depth was lost during the initial graphitisation, it was extracted again in October 2009 from air samples collected in 3 L stainless steel containers, and measured in January 2010. The samples collected at 68.05 and 72 m depth were extracted together with the lost 70 m sample, to check for any discrepancy between the first (May 2009) and the second (October 2009) extraction. The replicates agreed within the estimated uncertainty of the graphitisation at ANSTO.

From these $\Delta^{14}C$ values we convert to a mass conserving mole fraction $[^{14}CO_2]$ using

$$[^{14}CO_2] = \left(\frac{\Delta^{14}C}{1000}+1\right)\left(\frac{\delta^{13}C/1000+1}{-25/1000+1}\right)^2 \times A_{abs} \times [CO_2] \quad (3)$$

where we use $A_{abs} = 1.1764 \times 10^{-12}$ (Karlen et al., 1968). The values of $\delta^{13}C$ and $[CO_2]$ are known from measurements of NEEM firn air from CSIRO Aspendale. Note that in the $\Delta^{14}C$ notation used here the activity of the isotopic reference material is decay-corrected. Sample decay is included through a decay term in the firn air models (Trudinger et al., 1997).

The $\delta^{15}N_2$ data used as a tracer is corrected for the effect of thermal fractionation as described by Severinghaus et al. (2001), using additional borehole temperature measurements and the SIO firn air model.

2.4 Atmospheric histories of reference tracers

2.4.1 Combining different data series

When combining different data series they need to be placed on the same calibration scale. All ALE, GAGE and AGAGE data are on the same scale (SIO-2005). NOAA halocarbon data were converted to the most recent calibration scale (Geoff Dutton and Bradley Hall, personal communication).

Results of intercomparisons between AGAGE and NOAA halocarbon data were kindly provided to the NEEM gas group (Paul Krummel, personal communication); they are shown in Table 3. These values are used to bring all atmospheric histories on the NOAA scales used for the firn data. Two different comparison results are provided: comparisons of atmospheric data at a common measurement site (American Samoa) and comparisons of air tanks circulated around measurement labs (IHALACE: International HALocarbons in Air Comparison Experiment; Bradley Hall, personal communication). The comparisons are consistent for CFC-12 and CFC-113. Calibration offsets at American Samoa are time-dependent for CFC-11. For CH_3CCl_3 Samoa and IHALACE results are inconsistent (note that IHALACE tanks had a low CH_3CCl_3 mixing ratio), and different results are obtained with Electron Capture Detector (ECD) and Gas chromatographymass spectrometry (GCMS). As old trend data were obtained with ECD, GCMS measurements are not used for this species; a NOAA/AGAGE ratio of 1.035 is used for CH_3CCl_3.

Table 3. Calibration scale ratios (NOAA/AGAGE) for halocarbon species.

Species	Multiple sites[a,b] flask/in-situ	Samoa[a] in-situ/in-situ	IHALACE[c]	This study (prelim.IHALACE)	Scales	Comment
CFC-11	1.0100	1.0095	1.0058	1.0081	NOAA-1993/SIO-05	time dependent
CFC-11	1.0057	1.0080	-	1.0081	NOAA-1993/SIO-05	2007-2009 only
CFC-12	0.9973	0.9965	0.9978	0.9978	NOAA-2008/SIO-05	
CFC-113	1.0199	1.0251	1.0266	1.0215	NOAA-2003/SIO-05	
CH_3CCl_3	1.0339	1.0379	1.0572 / - [d]	1.0627 / 1.0526[d]	NOAA-2003/SIO-05	ECD detector
CH_3CCl_3	1.0158	-	1.0081 / - [d]	1.0081 / 1.0030[d]	NOAA-2003/SIO-05	GCMS detector

[a] Krummel, personal communication

[b] Based on Mace Head, Trinidad Head, Samoa and Cape Grim

[c] Hall, B.D., Engle, A., Mühle, J., Elkins, J. et al., Results from the International Halocarbons in Air Comparison Experiment (IHALACE), in preparation

[d] Ratios for tanks at 22 ppt and 18 ppt respectively

2.4.2 Description of the reconstructions

CO_2: Average of the Summit and Alert NOAA-ESRL monthly records are used from 6/1985 - 12/2008. For months when only data from either one of the stations is available that station is used, with a correction for the average Alert-Summit offset for that given month. Mauna Loa (MLO) NOAA-ESRL (7/1976-5/1985) and SIO (3/1958-6/1976) records are used for indicated periods with a latitudinal correction applied based on the mean of the modern day MLO-Summit and MLO-Alert offset. A months 2-4/1964 gap in the SIO MLO record is filled by linear interpolation.

Prior to MLO we use the Law Dome mean-annual 20-yr smoothed record (1832-1958) and the Law Dome 75-yr smoothed mean annual record (1800-1831) (Etheridge et al., 1996), corrected for the Law Dome-NEEM offset. For missing years data points are interpolated linearly. Both the value and the trend of the Law Dome-NEEM offset were determined for the period 1959-1978. In 1931 this results in the NEEM molar mixing ratio equaling Law Dome, so the inter-polar gradient goes to zero. For simplicity, beyond this point we simply set NEEM equal to Law Dome. A seasonal CO_2 cycle is added based on NEEM reconstructed monthly values for 1959-2008.

CH_4: Summit and Alert NOAA-ESRL monthly record from 6/1985-12/2008. For months when the Summit record is available, NEEM is set equal to Summit. For months where Summit record is unavailable, the NEEM reconstruction is based on Alert with a correction for the Summit-Alert offset for that month applied. Alert-Summit offsets show no significant trends with time.

Prior to the Alert record we use the Law Dome firn record (1978-1985) and the Law Dome ice core record (1800-1978) (Etheridge et al., 1998), scaled by 1.0124 to convert the data to the NOAA 2004 CH_4 calibration scale, and with a correction applied for the Law Dome-NEEM offset. The inter-polar gradient (IPG) is assumed to be constant at 45 ppb from 1800-1885 (Etheridge et al., 1998). For 1886-1985 it is assumed that the IPG is a function of both Law Dome $[CH_4]$ and $d[CH_4]/dt$. The IPG correction is tuned to the period 1986-1998 where direct atmospheric measurements are available and there is an appreciable growth rate $d[CH_4]/dt$. A seasonal CH_4 cycle proportional to the annual mean is added based on the reconstructed NEEM monthly values for 1986-2008.

$^{14}CO_2$: The atmospheric $^{14}CO_2$ record from Fruholmen, Norway, is used from 1/1963-6/1993 (Nydal and Lövseth, 1996). Atmospheric measurements from central Europe have been used from 6/1993-12/2008 (Vermunt and Jungfraujoch, Levin et al., 2008) and from 2/1959-12/1962 (Vermunt, Levin and Kromer, 2004).

Southern hemisphere atmospheric $^{14}CO_2$ measurements are used from 1954-1959 (Manning and Melhuish, 1994) with a correction of 30 ‰ on average to account for the interhemispheric gradient.

Prior to 1955 no direct atmospheric records exist and the reconstruction is equal to $\Delta^{14}CO_2$ reconstructed from dendrochronologically dated tree-ring samples (Reimer et al., 2004). The atmospheric $\Delta^{14}CO_2$ has been converted to a ppm scale using Eq. (3).

$\delta^{13}CO_2$: A $\delta^{13}CO_2$ reconstruction is used to convert $\Delta^{14}CO_2$ values from a permil scale to a ppm scale. The Alert CSIRO monthly record from 1/1990-6/2008 is used without correction, prior to which we use the Cape Grim air archive record (1978-1989) and the Law Dome ice core record (1800-1978) (Francey et al., 1999), with a correction applied for the Law Dome-NEEM offset.

CFC-11: Emission-based model results from Martinerie et al. (2009) before 7/1978. Mid Northern latitudes combined AGAGE monthly record 7/1978-3/2009. Overall scenario converted to NOAA scale with NOAA/AGAGE=1.0081 (IHALACE).

CFC-12: Mid Northern latitudes combined AGAGE

monthly record 1/1981- 3/2009 (early record ignored because of missing data and high inter-hemispheric gradient). 2D model results from Martinerie et al. (2009) before. Overall scenario converted to NOAA scale with NOAA/AGAGE=0.9978 (IHALACE).

CFC-113: Mid Northern latitudes combined AGAGE monthly record 6/1986- 3/2009 (early record ignored because of missing data and high inter-hemispheric gradient). Emission-based model results from Martinerie et al. (2009) before. Overall scenario converted to NOAA scale with NOAA/AGAGE=1.0215 (IHALACE).

SF_6: Barrow NOAA-ESRL combined (Geoff Dutton) monthly record 1/1999- 7/2009 (Barrow data for 1995-1998 ignored because of variable N/S gradient. Emission-based model results from Martinerie et al. (2009) before.

CH_3CCl_3: Mid Northern latitudes combined AGAGE monthly record 7/1978- 3/2009. Emission-based model results before 7/1978 (visual rescaling by 1.05). Overall scenario converted to NOAA scale with a NOAA/AGAGE ratio of 1.035 (Samoa data with ECD detection).

HFC-134a: Barrow NOAA monthly record 2/1995- 3/2009, Emission-based model results before 02/1995 (visual rescaling by 1.10).

The mid-latitude AGAGE data could not be extrapolated to high latitudes for halocarbons. First, meridional gradients in mixing ratio are highly time dependent. Second, the NOAA-ESRL mid Northern latitude site (Niwot Ridge) is a high altitude site, thus the effects of altitude and latitude on the mixing ratios cannot be separated.

2.4.3 Uncertainty estimates on atmospheric reconstructions

CO_2 uncertainties: 1985-2008: half the ALT/SUM offset, 1976-1985: half the ALT/SUM offset and the standard deviation of the ALT/MLO-NOAA offset, 1958-1976: half the ALT/SUM offset and the standard deviation of the ALT/MLO-SIO offset, 1930-1958: twice the 1σ Law Dome measurement uncertainty, the IPG uncertainty estimate, 1800-1930: three times the 1σ Law Dome uncertainty and the IPG uncertainty estimate. In each period the listed terms are added quadratically to estimate the total uncertainty.

CH_4 uncertainties: The CH_4 uncertainty is dominated by the uncertainty in the IPG estimate, which is large for CH_4. For this reason three independent reconstructions were made, and the uncertainty was taken as the maximum difference between the reconstructions. The first method is described in Sect. 2.4.2, a second method assumes the IPG is linearly related to the CH_4 mixing ratio, a third method uses the a linear regression analysis between atmospheric growth rate and IPG. The comparison leads to an uncertainty ranging from 5-42 ppb.

For halocarbons, expressing emission-related uncertainties in % results in an unrealistic zero uncertainty at the start date of emissions. Thus somewhat arbitrarily, a minimum absolute uncertainty (in ppt) was set to the present-day uncertainty. The large increase in uncertainty when switching from atmospheric records to emission based estimates is applied gradually (over about 2 years) for all halocarbon species.

CFC-11 uncertainties: 1995-2010: 1.5%, 1990-1994: 2.5%, 1978-1989: 3.5%, before 1978: 18%. The changes in uncertainty after 1978 roughly reflect an increasing bias between AGAGE and NOAA measurements when going back in time.

CFC-12 uncertainties: 1996-2010: 0.5%, 1981-1995: 2%, before 1981: 7.5%.

CFC-113 uncertainties: 1996-2010: 1%, 1986-1995: 2.5%, before 1986: 8.4%.

SF_6 uncertainties: 1999-2010: 1.5%, 1985-1998: 3.5% South. Hem. and 5% North. Hem., 1978-1984: 3.5% South. Hem. and 10% North. Hem., before 1978: 40%. The high uncertainty on emissions reflects mismatches between bottom-up and top-down estimates (WMO, 2007).

CH_3CCl_3 uncertainties: 2000-2010: 4.%, before 2000: 6%. These uncertainties are high compared to the 4.2% uncertainty on emissions from WMO (2007). They reflect the variability of the AGAGE/NOAA ratio and the dispersion around monthly mean values.

HFC-134a uncertainties: 2000-2010: 3.%, 1995-1999: 6% before 1995: 8.4%.

$\Delta^{14}CO_2$ uncertainties: direct atmospheric records are long compared to other tracers, and the largest source of uncertainty is latitudinal gradients, here estimated at 18 ‰.

2.7 Overall uncertainty estimation

We identify seven sources of uncertainty, all of which are assumed independent.

2.7.1 Analytical precision

We use the analytical precision as specified by the laboratories. In case of data from several laboratories for a single gas species, the largest of the specified uncertainties is used.

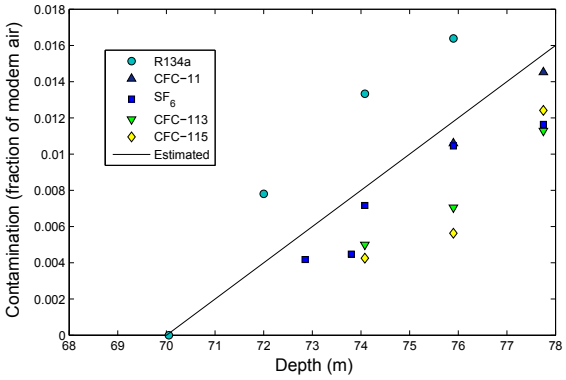

Fig. 2. Contamination as calculated from gas measurements, with in black the values used as the uncertainty estimate for contamination in all NEEM samples.

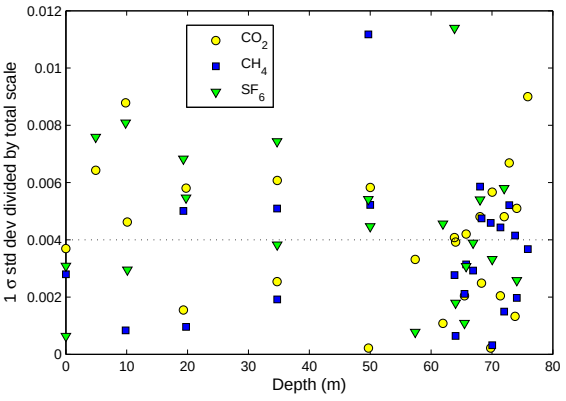

Fig. 3. Sampling uncertainties estimated from the standard deviation for each sampling depth. Standard deviations are divided by the total scale, meaning the highest minus the lowest measured mixing ratio.

Where there are multiple data points available for the same depth we additionally calculated the standard deviation between the data points. The assigned analytical uncertainty for a specific depth is taken as the larger of (1) the 1 σ standard deviation for that depth and (2) the (depth independent) lab specified uncertainty.

2.7.2 Uncertainty in atmospheric reconstruction

The uncertainties in the atmospheric reconstructions, as described in Sect. 2.4.3, are produced on a time scale. They are converted to a depth scale by running the uncertainties through the CIC firn air model with with near-finalised diffusivity tuning. This approach is valid since the diffusion model is linear with respect to the atmospheric input.

2.7.3 Sample contamination

Several halocarbon species should be absent at the deepest sampling level; we use these to estimate sample contamination. All contaminations are assumed to be with modern air, and expressed as a fraction of sample volume.

Figure 2 shows estimates of sample contamination from different gases, and our contamination estimate for NEEM as the black line

$$\frac{V_{\text{contam}}}{V} = \begin{cases} 0 & \text{if } z < 70\text{m} \\ 0.016 \times (z-70)/8 & \text{if } z \geq 70\text{m} \end{cases} \quad (4)$$

where V_{contam}/V is the fraction of the sample volume that comes from the modern atmosphere rather than from the open pores of the firn layer being sampled. Note that we do not make any corrections to the data, but rather assign an additional uncertainty to the deepest samples.

2.7.4 Sampling errors

The sampling procedure introduces errors which are not easily estimated. For CO_2, CH_4 and SF_6 we have data from several labs, as well as from both boreholes. We use these to estimate the influence of the sampling procedure.

We treat each gas species and borehole separately. First, we consider sampling depths for which we have data from at least two labs, and calculate the standard deviation of the data for that depth. The sampling uncertainty is estimated as the average of the obtained standard deviations. The assigned sampling uncertainty for a specific depth is taken as the larger of (1) the 1 σ standard deviation for that depth (when available) and (2) the average sampling uncertainty as described above.

The average sampling uncertainties thus obtained are:

CO_2:	0.32	ppm	(EU),	0.19	ppm (US)
CH_4:	1.8	ppb	(EU),	2.7	ppb (US)
SF_6:	0.035	ppt	(EU),	0.029	ppt (US)

The sampling error is found to be independent of depth (Fig. 3). For gases where we have data from only one lab an estimate is made based on the CO_2, CH_4 and SF_6 values. We find that the estimated sampling uncertainties divided by the total signal in the firn (i.e. the highest minus lowest mixing ratio), are comparable for all analysed data (Fig. 3). We use 0.4 % of the total scale as an estimate of sampling uncertainties.

2.7.5 Possible in-situ CO_2 artifacts

Due to the presence of organic material and (bi)carbonates in Greenland ice there is the possibility of in-situ CO_2 contamination artifacts. We observe a CO_2 model-data mismatch in the deepest firn on the order of 5 ppm (Fig. 4a and Fig. 3a of the main text). For this reason we include the following uncertainty for CO_2:

$$u_{\mathrm{CO_2}}(z) = \begin{cases} 0 & \text{if } z < 68\mathrm{m} \\ 0.5 \times (z - 68) & \text{if } z \geq 68\mathrm{m} \end{cases} \quad (5)$$

This uncertainty estimate also covers the possibility of CO_2 enrichment due to close-off fractionation of the CO_2/air ratio, which occurs at the same depths (Severinghaus and Battle (2006) could not exclude a 1 ‰ effect).

In situ cosmogenic production of $^{14}CO_2$ from nuclear spallation is known to occur in the top few meters of the firn. Though most will be lost due to firn ventilation, some could be retained in the ice matrix and released only at depth. The deepest sample has a $\Delta^{14}CO_2$ of 44.9 ‰. The CO_2 mean age at this depth is from the late 1950s, for which our atmospheric reconstruction gives a atmospheric value of around 100 ‰. There is therefore no indication that the cosmogenically produced $^{14}CO_2$ has been released from the ice matrix at depth. The uncertainty related to in situ CO_2 production, however, has been translated into an uncertainty in $\Delta^{14}CO_2$ (~ 13 ‰ in the deepest firn).

2.7.6 Undersampling of the seasonal cycle in CO_2

The atmospheric reconstructions used in this study have a monthly resolution. In the top layers undersampling of the seasonal cycle leads to a potential misfit between modeled profiles and data. We include this effect in the following way. First we linearly interpolate the CO_2 reconstruction to a $\frac{1}{2}$ month resolution. Then we run the CIC model (with nearly finalised tuning) twice, with final dates at $\pm\frac{1}{2}$ month around the firn air sampling date. The uncertainty estimate is set to half the difference between these two runs.

This test is done for all gases that vary seasonally; the effect is found to be only significant for CO_2.

2.7.7 SF_6 offset between the EU and US holes

We observe an unexplained ~ 0.25 ppt offset between the EU and US boreholes for SF_6 in the depth range $z \sim 5-50$ m. We can exclude differences in gas age, incomplete flask flushing, sample contamination, procedural blanks and bladder outgassing as the origin. Since we found no objective reason to reject data from either hole, we account for the discrepancy by assigning an additional errorbar to the SF_6 data from both holes. The magnitude of the assigned uncertainty can be found in the Excel sheet included with this supplement. We have no reason to suspect other tracers are affected by a similar offset.

3 Modeling firn air transport at NEEM

3.1 Tuning of the diffusivity profile

The diffusion coefficient ratios γ_X for both trace gases and isotopic ratios that are used in this study are listed in Tables 4 and 5. The tables also include gases that are not directly used here, but might be of interest to firn air modeling studies in general.

First, all diffusion coefficients reported here are the binary diffusivity of the gas into air. The values are presented as ratios to the diffusivity of CO_2-air. Thus the values presented are unitless. This convention is followed even in the case of isotopic species.

Second, experimental values reported by the Matsunaga group are used where possible, extrapolated to -28.9°C. Where this is not possible, calculated values are given using the method of Chen and Othmer (1962). The latter are identified in Table 4 with an asterisk (*). Values for isotopic species are calculated using the "square root of the ratio of the reduced masses" law:

$$D_{\text{X-air}} = \sqrt{\frac{M_{\text{X}}^{-1} + M_{\text{air}}^{-1}}{M_{\text{Y}}^{-1} + M_{\text{air}}^{-1}}} D_{\text{Y-air}} \quad (6)$$

where X refers to the minor isotopic species, and Y to the major isotopic species. The mass M is calculated for air by assuming that water vapor in the firn is saturated at -28.9°C. The mass of dry air is calculated from the 1976 US Standard Atmosphere, with a small adjustment for the increase in the mass of dry air due to a mixing ratio update for the anthropogenic gases (CO_2 385 ppm, O_2 20.9367%, N_2 78.088%). This results in an air mass M_{air} of 28.9589 $\mathrm{g\,mol^{-1}}$.

Third, an isotopic substitution in a gas molecule affects the diffusivity by changing the mass. Each isotopologue must be modeled separately, as a trace gas diffusing into a air, each with its own diffusivity. Then, the customary delta value must be computed from the modeled depth profiles of the two isotopologues.

Fourth, to relate the values of diffusivities for isotopic species (i.e. species with well defined isotopic substitutions) to the values for non-isotopic species (i.e. having no specified isotopic substitutions and a mass corresponding to the sum of all isotopes/isotopologues, weighed by their natural abundance) in an internally consistent way, we first calculate the diffusivity ratio of the major isotopologue to the non-isotopic species (for which experimental values are available) using Eq. (6). Second, we calculate the diffusivity ratio of the minor isotopologue to the major one, again using Eq. (6). The differences between the major isotopologue and the non-isotopic species are not significant in most cases, but we nonetheless calculated them for the sake of conceptual clarity.

Fifth, the non-isotopic species are generally not used to calculate delta values ($\Delta^{14}C$ is an exception). Rather, the species in the denominator in the delta calculation is generally a specific isotope, usually the major isotope, such as ^{1}H, ^{12}C, ^{14}N, or ^{16}O. Also, Table 4 only presents three or four significant figures for the diffusivities for non-isotopic species. This is not usually sufficient for delta calculations.

Table 4. Diffusion coefficients of several trace gases at the NEEM site as used in this study. $T = 244.25$ K, $p = 745$ mbar. Values are based on Matsunaga et al. (1998, 2002a,b, 2005, 2006, 2007, 2009), unless marked with an asterisk. For those cases Chen and Othmer (1962) is used. For all these trace gases we use the natural isotopic abundance of the constituent atoms when calculating the molar mass.

Gas (X)	γ_X
CO_2	1.000
CH_4	1.367
N_2O	0.981
SF_6	0.554
H_2	4.694
CFC-11	0.525
CFC-12	0.596
CFC-113	0.453
CFC-114	0.496
CFC-115	0.532
HCFC-22	0.710
HCFC-123	0.509
HFC-134a	0.630
HFC-32	0.866
HCFC-124	0.538
HFC-125	0.589
HFC-143a	0.647
HFC-43-10mee	0.383
CH_3Br	0.736
CH_3I	0.658
CF_4	0.823
C_3H_8	0.649
C_3H_6	0.671
CH_3OCH_3	0.827
$C_2H_5OC_2H_5$	0.525
CH_3CCl_3	0.485
CCl_4	0.470
CH_2Cl_2	0.709
$CHCl_3$	0.595
C_2H_5Cl	0.743
CH_2ClCH_2Cl	0.600
CH_2CCl_2	0.641
$CHClCCl_2$	0.583
CH_3Cl	0.789 *
CO	1.250 *
Hg	0.868 *
H_2O	1.374 *
N_2	1.275 *
O_2	1.302 *
C_5H_{12}	0.505 *
He	4.780 *
Ne	2.140 *
Ar	1.230 *
Kr	0.962 *
Xe	0.835 *

Table 5. Diffusion coefficients for specific isotopologues. To model isotopic ratios both major and minor abundance isotopologues are to be modeled separately. Values calculated using natural abundance diffusion coefficients listed in Table 4 in combination with Eq. (6) at $T = 244.25$ K and $p = 745$ mbar.

Isotopologue (X)	γ_X	for use in
HD	3.895386	δD
HH	4.693994	δD
$^{13}CH_4$	1.340806	δ^{13}C
$^{12}CH_4$	1.366969	δ^{13}C
CDH_3	1.340469 **	δD
CH_4	1.366676 **	δD
$^{14}CO_2$	0.991368 ***	Δ^{14}C
CO_2	1.000000 †	Δ^{14}C
$^{13}CO_2$	0.995613 ***	δ^{13}C
$^{12}CO_2$	1.000048 ***	δ^{13}C
$^{12}C^{18}O^{16}O$	0.991401	δ^{18}O
$^{12}C^{17}O^{16}O$	0.995648	δ^{17}O
$^{12}C^{16}O^{16}O$	1.000089	δ^{17}O and δ^{18}O
$^{12}C^{18}O$	1.228754	δ^{18}O
$^{12}C^{17}O$	1.239117	δ^{17}O
$^{12}C^{16}O$	1.250172	δ^{17}O and δ^{18}O
$^{15}N^{14}N^{16}O$	0.976915 ‡	$^{\alpha}\delta^{15}$N, $^{\beta}\delta^{15}$N
$^{18}ON_2$	0.972718	δ^{18}O
$^{17}ON_2$	0.976884	δ^{17}O
$^{16}ON_2$	0.981239	$^{\alpha}\delta^{15}$N, $^{\beta}\delta^{15}$N, δ^{17}O,δ^{18}O
$^{15}N^{14}N$	1.263893	δ^{15}N
$^{14}N^{14}N$	1.275084	δ^{15}N
$^{18}O^{16}O$	1.283719	δ^{18}O
$^{17}O^{16}O$	1.292637	δ^{17}O
$^{16}O^{16}O$	1.302087	δ^{17}O and δ^{18}O
^{22}Ne	2.087122	δ^{22}Ne and δNe/Ar
^{20}Ne	2.145608	δ^{22}Ne
^{40}Ar	1.229952	δ^{40}Ar
^{38}Ar	1.243488	δ^{38}Ar
^{36}Ar	1.258324	δ^{40}Ar, δ^{38}Ar, Kr,Xe,Ne
^{86}Kr	0.958741	δ^{86}Kr
^{84}Kr	0.961616	δ^{84}Kr and δKr/Ar
^{82}Kr	0.964621	δ^{86}Kr and δ^{84}Kr
^{136}Xe	0.832366	δ^{136}Xe
^{132}Xe	0.834581	δ^{132}Xe and δXe/Ar
^{129}Xe	0.836327	δ^{136}Xe and δ^{132}Xe

** Includes mass effect of ^{13}C-containing isotopologue in its natural abundance, in keeping with convention for reporting deuterium data

*** Includes mass effects of ^{17}O- and ^{18}O- containing isotopologues in their natural abundances, in keeping with conventions for reporting ^{14}C and ^{13}C data.

† Convention for reporting ^{14}C has it as the ratio to non-isotopic (i.e. natural abundance) C

‡ This value applies to both isotopomers having the ^{15}N at the central and terminal positions .

So all δ calculations should use the diffusivities in Table 5, which have 6 or 7 significant figures.

3.2 Model description

Below follows a brief description of the different firn air models in alphabetical order.

3.2.1 CIC model

A complete description of the CIC model and tuning routine can be found in Buizert (2012).

3.2.2 CSIRO model

The CSIRO firn model is based on the model described by Trudinger et al. (1997). Since then it has been rewritten into Fortran90, flux smoothing is no longer used, and an implicit time stepping, the same as that used by Rommelaere et al. (1997), has replaced the Euler predictor-corrector scheme. The time step used here was 0.1 years up to 2000 then 0.01 years to the end. An exponential eddy diffusion flux has been added following Severinghaus et al. (2001) to account for convective mixing near the surface, with 2 tuned parameters (surface magnitude and scale depth). A genetic algorithm (from Haupt and Haupt (1998)) is used to calibrate the diffusivity versus open porosity and the eddy diffusion parameters. We adjust the open porosity values corresponding to about 12 specified diffusivity values to give the diffusivity profile, with cubic splines used to interpolate between these points, and diffusivity capped at 500 $\mathrm{m^2 yr^{-1}}$ (0.158×10^{-4} $\mathrm{m^2 s^{-1}}$) near the surface. We only allow monotonic solutions (as defined by the points) but the cubic splines, which match the gradient of adjacent splines at each point, can often lead to non-monotonic diffusivity vs open porosity profiles. We therefore penalise oscillatory behaviour with an additional term added to the cost function that is the squared difference between a line integral following the cubic spline and a line integral for linear interpolation between the points. Any negative diffusivity values are set to zero. The genetic algorithm does not require an initial guess, but does require a range for each parameter. The ranges were initially chosen as representative of values for other calibrated sites, and extended if solutions from the genetic algorithm with low values of the cost function collected near either end of the range.

3.2.3 INSTAAR model

The INSTAAR 1-D firn gas transport model was originally based on a model described in Severinghaus and Battle (2006), but has evolved substantially. The model has fixed coordinates with only the gases moving through the firn matrix. The NEEM firn is parameterised with 1 m deep boxes between -0.5 and 59.5 m (top model box is half-free air, half-firn), and with 0.25 m deep boxes below 59.5 m.

For each box, the model keeps track of the gas content in the open porosity as well as in the ice-enclosed bubbles, but the gas mixing ratios are only tracked in the open porosity part. Rate of total downward air advection is determined from the air content of ice below close-off and the ice accumulation rate. From mass conservation, the total downward air advection should be the same at each level. The rate of advection in the open porosity at each level is therefore calculated as the total downward air advection rate minus the advection of air in the bubbles at that level (found from bubble air content and ice accumulation rate).

Unlike the model described in Severinghaus and Battle (2006), the INSTAAR model does not have any fundamental differences in the mechanisms of gas movement between the diffusive zone and the lock-in zone. In the INSTAAR model the reduced gas movement in the lock-in zone is achieved simply through adjusting the overall effective gas diffusivities to lower levels.

The model includes a seasonal temperature cycle and calculates firn temperature in each model box in the same way as the Severinghaus and Battle (2006) firn model.

The model uses explicit time stepping. To avoid computational instability the time step is always chosen to be smaller than $\Delta t < (\Delta z)^2/3D_{\mathrm{total}}$, where Δt is the time step, Δz is the box size in m, and D_{total} is the total effective diffusivity in $\mathrm{m^2 s^{-1}}$. For all gases except H_2, this time step was set to 11,119 s (3.5×10^{-4} yr). For H_2, which has a much higher molecular diffusivity, the time step was set to 3,156 s (1×10^{-4} yr).

The equation used to calculate flux of gas X between two adjacent boxes due to molecular diffusion and gravity at each time step is as follows:

$$J_{X;\text{molec-grav}(i)} = -\gamma_X D^0_{\mathrm{CO_2}} \tau_i^{-1} s_{\text{op; mid}} \times \left(\frac{C_{i+1}-C_i}{\Delta z_{\text{mid}}} - \frac{\Delta M g}{RT_i} \frac{C_{i+1}+C_i}{2} \right) \quad (7)$$

Here $J_{X;\text{molec-grav}(i)}$ is the gas flux between box i and $i+1$ (in units of e.g., $\mathrm{ppm m s^{-1}}$). This can be thought of as the volume of the pure gas moving across a unit area of the boundary between boxes per unit time. $\gamma_X D^0_{\mathrm{CO_2}}$ is the free-air diffusivity of gas X at the boundary between box i and $i+1$ in $\mathrm{m^2 s^{-1}}$, re-calculated at each time step to take into account firn temperature variations; τ_i^{-1} is the tuned dimensionless multiplier (or inverse tortuosity) to the free air diffusivity for box i. $s_{\text{op; mid}}$ is the open porosity ($\mathrm{m^3/m^3}$) at the boundary between the two boxes. This is included because the flux should be proportional to the open porosity. C_i is the gas mixing ratio in box i (e.g., in ppm), Δz_{mid} is the distance (m) between the middles of box i and box $i+1$, ΔM is the molar mass difference ($\mathrm{kg mol^{-1}}$) between the gas and bulk air, g is the acceleration due to gravity ($\mathrm{m s^{-2}}$), R is

the universal gas constant ($\mathrm{J mol^{-1} K^{-1}}$) and T_i is the firn temperature (K) at the boundary between boxes i and $i+1$.

The basic form of the equation used to calculate the gas flux due to eddy diffusion or turbulent mixing is:

$$J_{\mathrm{eddy}(i)} = -D_{\mathrm{eddy}(i)} s_{\mathrm{op;\,mid}} \frac{C_{i+1} - C_i}{\Delta z_{\mathrm{mid}}} \tag{8}$$

where $J_{\mathrm{eddy}(i)}$ is the gas flux due to eddy diffusion ($\mathrm{ppm m^3 m^{-2} s^{-1}}$) and $D_{\mathrm{eddy}(i)}$ is the tuned eddy diffusivity ($\mathrm{m^2 s^{-1}}$) for box i.

Gas fluxes due to advection and flux of air into newly formed bubbles are also calculated at each time step. All of these fluxes are corrected to STP volumes (to account for varying temperature and pressure in the firn column) and are added to find the total flux of gas into the box (J_{in}) and the total flux of gas out of the box (J_{out}). The time derivative of the gas mixing ratio in box i is then calculated as:

$$\frac{\Delta C_i}{\Delta t} = \left(\frac{J_{\mathrm{in}} - J_{\mathrm{out}}}{s_{\mathrm{op}(i)} \Delta z_i} \right) \tag{9}$$

where s_i is the open porosity in the box and Δz_i is the vertical length of box i.

The effective diffusivities in the INSTAAR model were manually tuned to optimise the fit to the suite of 10 gases. The initial guess for effective molecular diffusivities used the free-air diffusivity in the surface box, with effective diffusivities for CO_2 declining linearly to 2.0×10^{-9} $\mathrm{m^2 s^{-1}}$ at 64m and staying constant beyond 64 m. The initial guess for eddy diffusivity set the eddy diffusivity equal to molecular diffusivity for CO_2 in the surface box, and prescribed an exponential decrease with depth using an e-folding depth of 4 m. Below the depth where eddy diffusivity dropped to 1.0×10^{-8} $\mathrm{m^2 s^{-1}}$ it was held constant at this value.

3.2.4 LGGE-GIPSA model

The LGGE-GIPSA model is described in detail in (Witrant et al., 2011).

3.2.5 OSU model

The OSU firn air model is a finite-difference diffusion model based on the mixing ratio equations of Trudinger et al. (1997), Eqs. (A9) and (A13). An eddy-diffusion term is added to represent surface convection Kawamura et al. (2006) and to account for LIZ mixing that is not due to molecular diffusion.

The model uses an implicit Crank-Nicholson numerical scheme, which makes it stable over a large range of depth increments and time steps. Because of this, at the model time step of 0.005 years and depth resolution of 0.1 m, the flux smoothing technique of Trudinger et al. (1997) is not employed.

Vertical advection of the firn is accounted for by shuffling boxes down at every time step, rather than moving the reference frame (Schwander et al., 1993). An evenly spaced depth scale is used, which makes computation of the diffusion equation simpler but complicates shifting boxes as the firn densifies and the equally spaced boxes contain less and less air. To deal with this, the vertical displacement of the air at every depth and every time step is calculated. The vertical air velocity used to compute displacement differs from the ice velocity (Rommelaere et al., 1997) and is given by the equation of Buizert (2012). This creates a new mixing-ratio profile with different depth values which is then interpolated back onto the fixed grid, and assigned the correct firn properties at each depth. The value of the top box is set to the atmospheric mixing ratio for the current time step during this process.

Bubble compression is accounted for only in the LIZ, because above this zone it is assumed that the pressure in the open porosity is equal to atmospheric pressure. Below the top of the LIZ, the model uses the following correction to account for the greater amount of air in the open porous volume:

$$s^*_{\mathrm{op}}(z) = s_{\mathrm{op}}(z) \frac{\rho(z)}{\rho_{\mathrm{LID}}} \tag{10}$$

where $s_{\mathrm{op}}(z)$ is the true open porosity at depth z, $\rho(z)$ is the density (Eq. (1)), and ρ_{LID} is the density at the lock-in depth, i.e. at the top of the LIZ. Bubble compression of the closed porosity is ignored since this is an open porosity model. The diffusivity parameterisation of Schwander et al. (1993) is used as a first estimate, but a second-order porosity dependence was added later to improve the fit. The form of the final diffusivity profile is:

$$D_X(z) = D^0_X \left[g_1 + g_2 s_{\mathrm{op}}(z) + g_3 s^2_{\mathrm{op}}(z) \right] \tag{11}$$

Values for constants g_1, g_2 and g_3 were manually adjusted to minimise the total root mean squared error of the model-data mismatch for all tracers, including δ^{15}N. Final values are listed in Table 6. Where molecular diffusivity goes to zero in the LIZ, the model uses a synthetic exponential decrease to prevent numerical instabilities. This takes the form:

$$D_X(z) = g_4 + (D_X(z_{\mathrm{LID}}) - g_4) e^{-g_5 (z - z_{\mathrm{LID}})}, \quad \text{for } z > z_{\mathrm{LID}} \tag{12}$$

where g_4 is some relict molecular diffusivity and z_{LID} is the lock-in depth. Dispersive eddy diffusivity in the lock-in zone is parameterised by the following exponential:

$$D_{\mathrm{eddy}}(z) = g_6 e^{g_7 (z - z_{\mathrm{LID}})}, \quad \text{for } z > z_{\mathrm{LID}} \tag{13}$$

where again g_6 and g_7 were iteratively adjusted to provide the best fit to the data.

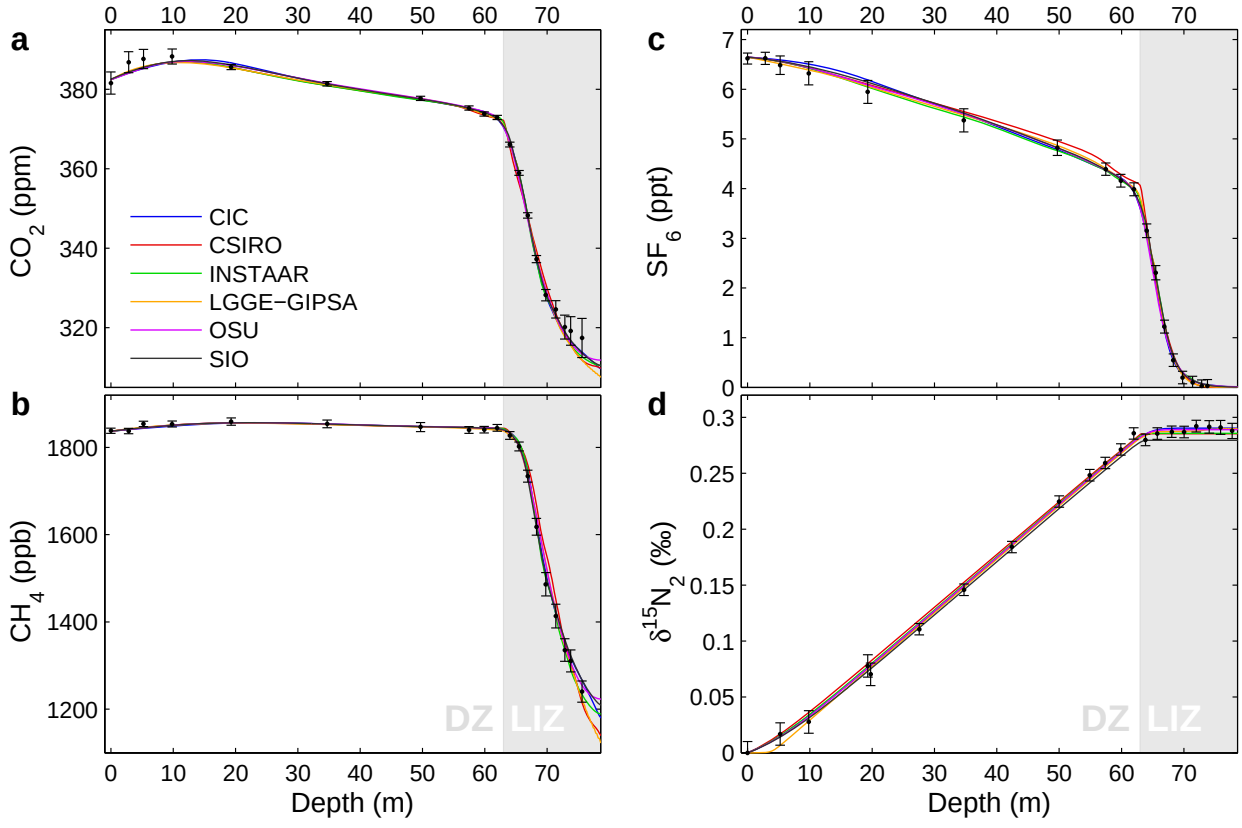

Fig. 4. (a–d) Modeled profiles for all 4 tracers from the US borehole. With the exception of **(d)** data have been gravity corrected and the models are run with gravity turned off. Errorbars correspond to full 1σ uncertainty as defined in Sect. 2.7.

Table 6. Constants used in the OSU diffusivity tuning for the EU borehole

constant	value	unit
g_1	- 0.209	
g_2	1.515	
g_3	0.53	
g_4	3.17×10^{-10}	$m^2 s^{-1}$
g_5	1.82	m
g_6	3.17×10^{-9}	$m^2 s^{-1}$
g_7	0.11	m

3.2.6 SIO model

The Scripps Institution of Oceanography (SIO) firn air model follows generally those of Schwander et al. (1993), Rommelaere et al. (1997), Severinghaus and Battle (2006), and Severinghaus et al. (2010) (hereafter S2010). Slight differences from the model of S2010 include the following. (i) Barometric pressure increases with depth, according to the isothermal barometric equation set with the initial mean-annual temperature, (ii) gravity is set to zero within the lock-in zone, (iii) molecular and eddy diffusion both continue throughout the LIZ, and (iv) the LIZ grid spacing is calculated with the air advection velocity until the close-off density and thereafter with the firn velocity, whereas S2010 calculated it with the firn velocity in the entire LIZ.

The main differences between the SIO model and the other models in the present intercomparison are:

1) The model has a parallel heat transport model within it that predicts temperature as a function of depth and time. For the NEEM intercomparison runs, the temperature model was disabled, but the full model was used to make thermal diffusion corrections to NEEM firn air δ^{15}N and δ^{86}Kr data used as inputs.

2) The SIO model treats downward air advection in the LIZ by shifting concentrations down by one grid point every 0.5 yr, rather than with explicit advection schemes. The grid points are spaced apart by distances such that the air advection velocity w_{air} would transport the air that distance in 0.5 yr. This scheme minimises the numerical diffusion common to upwind advection schemes.

The inverse tortuosity profile $\tau^{-1}(z)$ is tuned using a generalised least square method. The initial guess $\tau_o^{-1}(z)$ is a parameterisation by J. Schwander. Subsequent profiles are

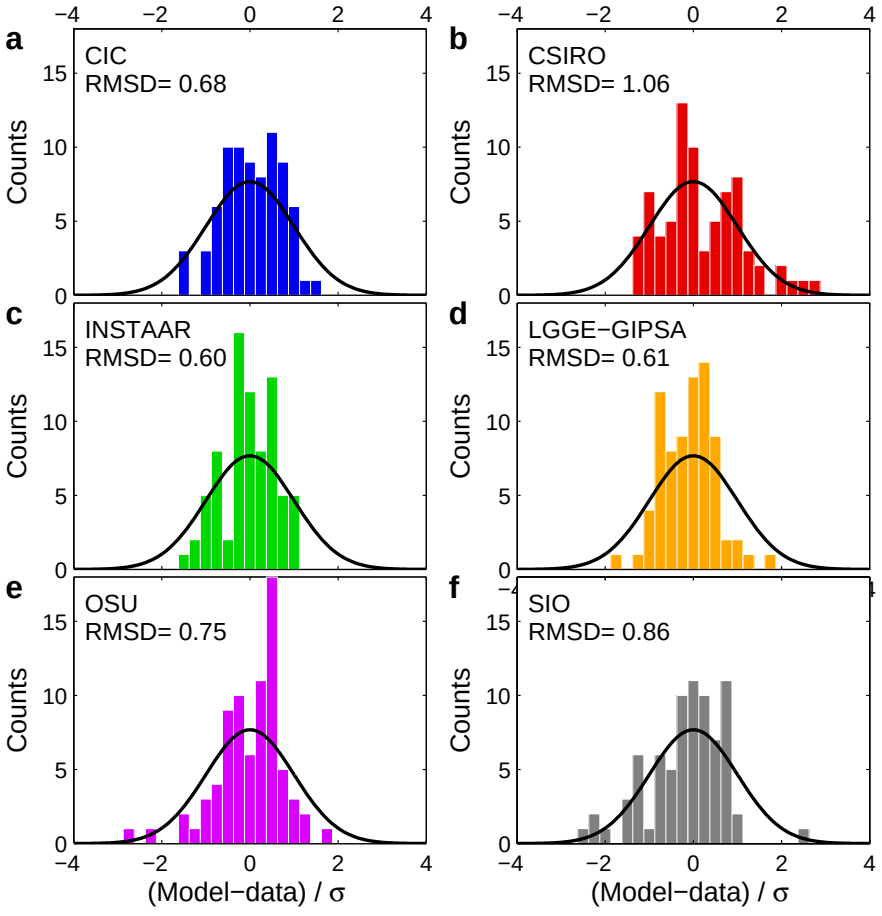

Fig. 5. (a–f) Histogram of $(m_i - d_i)/\sigma_i$ for the firn air transport models in this study using the US borehole data. The black curve gives a Gaussian distribution of width $\sigma = 1$, normalised to have equal surface to the histogram. The RMSD is calculated with Eq. (3) of the main article.

determined using:

$$\tau^{-1}(z) = \tau_o^{-1}(z) + \sum_{i=1}^{N} h_i * f_i(z) \qquad (14)$$

$$\begin{aligned} f_i(z) &= 0 && z < i\Delta z \\ f_i(z) &= a(z - i\Delta z)/\Delta z && i\Delta z < z < (i+1)\Delta z \\ f_i(z) &= a((i+2)\Delta z - z)/\Delta z && (i+1)\Delta z < z < (i+2)\Delta z \\ f_i(z) &= 0 && z > (i+2)\Delta z \end{aligned}$$

We use an amplitude $a = 10^{-6}$ m^{2}s^{-1} between 0 and 60m, and $a = 10^{-8}$ m^{2}s^{-1} between 60 and 80m. The half width Δz was set to $\Delta z = 0.5$ m. The coefficients h_i are optimised using a least square regression to minimise the RMS misfit given in Eq. (3) of the main text.

Near the surface, the eddy diffusivity due to wind pumping is parameterised by an exponential:

$$D_{\mathrm{eddy}}(z) = D^0_{\mathrm{eddy}} \exp\left(-\frac{z}{H}\right) \qquad (15)$$

$D^0_{\mathrm{eddy}} = 1.6e^{-5}$ m^{2}s^{-1} and $H = 5$ m are tuned to fit the δ^{15}N and δ^{86}Kr data, corrected for thermal fractionation.

In the lock in zone, the balance between molecular diffusion (affecting each gas differently) and dispersion (affecting all the gases proportionally) is determined by a single coefficient α varying between 0 and 1, rather than by having a free dispersion diffusivity profile, which is largely underconstrained. The molecular diffusivity is then:

$$D_X(z) = (1-\alpha)\frac{D^0_X}{\tau(z)} \qquad (16)$$

And the dispersion, included as an eddy diffusivity, is:

$$D_{\mathrm{eddy}}(z) = \alpha \frac{D^0_{\mathrm{CO_2}}}{\tau(z)} \qquad (17)$$

Here $D^0_{\mathrm{CO_2}}$ is used as the reference, all gases experience the same $D_{\mathrm{eddy}}(z)$. The optimum α was $\alpha_{\mathrm{EU}} = 0.27$ for the EU hole, and $\alpha_{\mathrm{US}} = 0.35$ for the US hole.

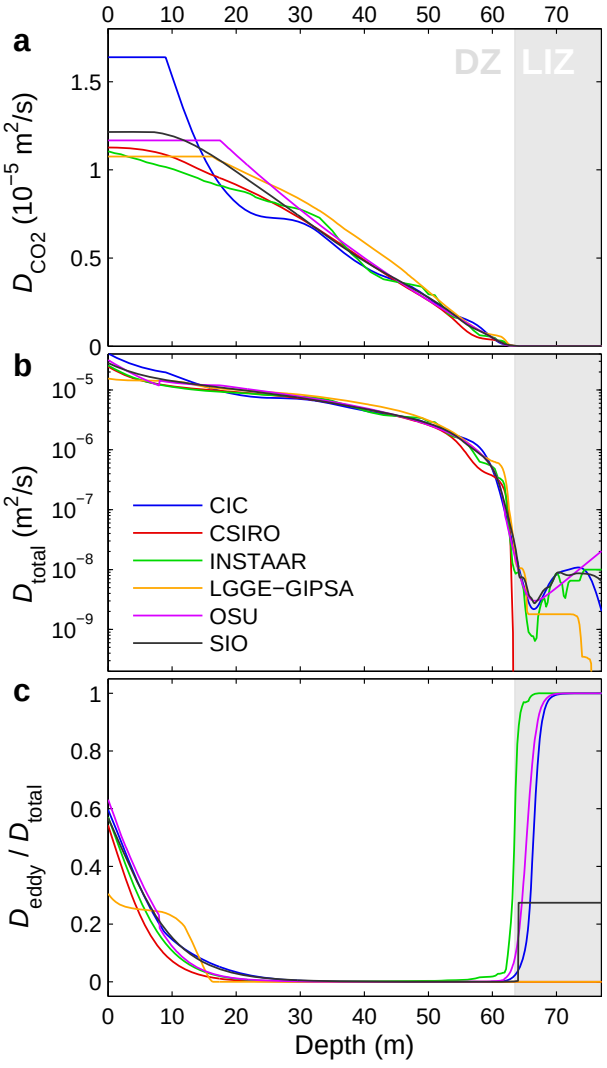

Fig. 6. **(a)** CO_2 molecular diffusivity profile with depth $D_{CO_2}(z)$ for the US borehole. **(b)** Semi-log plot of the total CO_2 diffusivity profile $D_{total}(z) = D_{CO_2}(z) + D_{eddy}$. **(c)** Plot of $D_{eddy}(z)/D_{total}(z)$. The eddy diffusion near the surface corresponds to the convective mixing, in the LIZ some of the models have included dispersive mixing.

3.3 Fit of modeled profiles to the data

The firn models were tuned to the US borehole using four different tracers: CO_2, CH_4, SF_6 and $\delta^{15}N_2$. The fit to the data is shown in Fig. 4. As for the EU borehole we find a mismatch at depths $z > 70$m for CO_2 (Fig. 4A); the feature is reproduced consistently by all the firn air models.

Fig. 5 shows histograms of $(m_i - d_i)/\sigma_i$, where the index i goes over all the 77 data points of the US borehole. Black curves show a Gaussian distribution of width $\sigma = 1$ and a surface area equal to that of the histogram. Most models perform better for the US borehole in terms of the RMSD, which is due to the fact that there are fewer tracers for the US borehole.

Table 7. Mean age, median age, Full Width at Half Maximum and Spectral Width at the lock-in depth ($z = 63$ m) and bottom of the LIZ ($z = 76$ m) for the US borehole. All values given in years. We use the 2σ standard deviation divided by the mean ($2\sigma/\mu$) as a measure of the spread in model results.

Model	Mean	Median	FWHM	Δ
		$z = 63$ m		
CIC	8.3	6.7	7.2	4.0
CSIRO	7.3	6.1	6.4	3.1
INSTAAR	7.7	6.2	6.6	3.7
LGGE-GIPSA	12.2	8.2	8.5	8.3
OSU	8.2	6.6	7.1	4.0
SIO	8.1	6.5	7.0	3.9
$2\sigma/\mu$	0.41	0.23	0.21	0.84
		$z = 76$ m		
CIC	61.6	58.1	39.8	14.6
CSIRO	60.2	59.1	6.4	3.1
INSTAAR	63.5	60.5	39.8	14.0
LGGE-GIPSA	68.8	66.2	34.6	12.3
OSU	62.1	58.9	40.3	14.2
SIO	62.5	59.0	41.5	14.8
$2\sigma/\mu$	0.09	0.10	0.81	0.74

4 Model intercomparison and discussion

4.1 Diffusivity profiles

Figure 6a shows the reconstructed molecular diffusivity profiles for CO_2. In Fig. 6b the total diffusivity $D_{total}(z) = D_{CO2}(z) + D_{eddy}$ for CO_2 is plotted on a semi-log scale. As for the EU borehole we observe that the models require a non-vanishing diffusivity within the LIZ to fit the data.

4.2 Gas age distributions

Figure 7 compares age distribution densities for the models at the lock-in depth ($z = 63$ m) and near the deepest sample ($z = 76$ m) on the US hole. Table 7 gives some characteristics of the distributions. For the US hole the spread in the calculated mean ages is larger than for the EU hole. This large spread is mostly due to the LGGE-GIPSA model, which stands out as having a wider and flatter age distribution. We attribute the larger spread found in modeled US borehole mean ages to the fact that it has fewer tracers. The CSIRO age distribution at $z = 76$ m is very narrow compared to the other models, due to the absence of LIZ diffusion in the US hole.

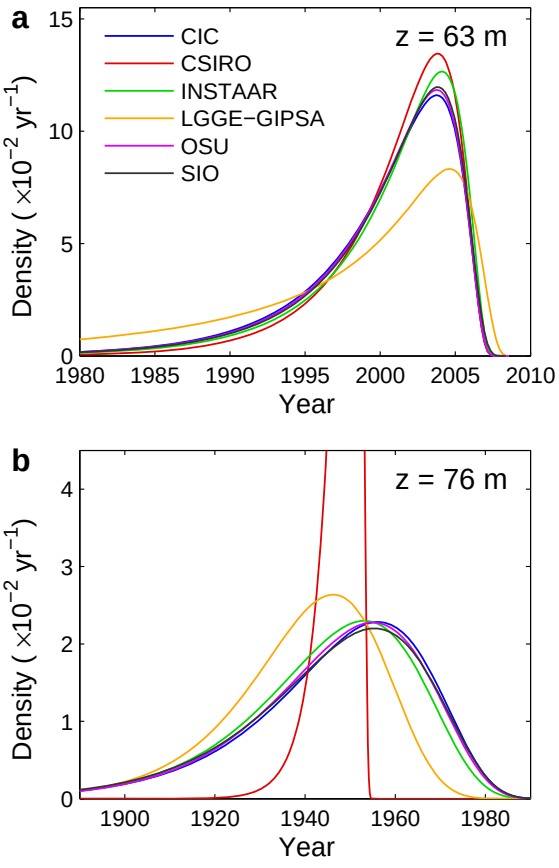

Fig. 7. US borehole modeled age distribution densities for **(a)** $z = 63$m (lock-in depth) and **(b)** $z = 76$m (deepest sample). On the horizontal axis are calendar years C.E.; decimal sampling year is 2008.54 (i.e. mid July). Age distributions are generated by applying a surface forcing which is unity for $0.2 \leq t < 0.4$ yr, and zero elsewhere.

4.4 Synthetic diagnostic scenarios

Table 8 provides detailed specifications on how the diagnostic scenarios are run in the models.

For Scenario I we model the mole fractions of $[^{12}CO_2]$ and $[^{13}CO_2]$ separately. We let the atmosphere have the property

$$^{13}R_{\text{std}} = \left.\frac{[^{13}CO_2]}{[^{12}CO_2]}\right|_{\text{std}} = 1 \qquad (18)$$

or $[^{12}CO_2] = [^{13}CO_2]$. We use the same atmospheric input file to force both isotopologues. The fractionation with depth is then given as

$$\delta^{13}CO_2(z) = \left(\frac{[^{13}CO_2](z)}{[^{12}CO_2](z)} - 1\right) \times 10^3 \text{ ‰} \qquad (19)$$

Fig. 8 shows the scenario comparison for the US borehole. We observe similar model differences as on the EU borehole. Scenario IV is identical to the EU borehole as we assume the same density profile and accumulation rate.

Notation

A	Accumulation rate (myr^{-1} ice equivalent)
A_{abs}	Absolute ^{14}C abundance (1.1764×10^{-12})
C	Mixing ratio (molmol^{-1})
D_{eddy}	Eddy diffusion coefficient ($\mathrm{m}^2\mathrm{s}^{-2}$)
D_X	Diffusion coefficient of gas X ($\mathrm{m}^2\mathrm{s}^{-2}$)
D_X^0	Free air diffusion coeff. of gas X ($\mathrm{m}^2\mathrm{s}^{-2}$)
d_i	Data point i
g	Gravitational acceleration (9.82 ms^{-2})
J	Trace gas flux ($\mathrm{molmol}^{-1}\mathrm{ms}^{-1}$)
M_{air}	Molar mass of air (kgmol^{-1})
M_{X}	Molar mass of gas X (kgmol^{-1})
m_i	Modeled value for data point i
p	Air pressure (Pa)
R	Molar gas constant (8.314 $\mathrm{Jmol}^{-1}\mathrm{K}^{-1}$)
RMSD	Root Mean Square Deviation
s	Total porosity ($\mathrm{m}^3\mathrm{m}^{-3}$)
s_{co}	Mean close-off porosity ($\mathrm{m}^3\mathrm{m}^{-3}$)
$s_{\text{op(cl)}}$	Open (closed) porosity ($\mathrm{m}^3\mathrm{m}^{-3}$)
s^*_{op}	Effective open porosity ($\mathrm{m}^3\mathrm{m}^{-3}$)
T	Absolute temperature (K)
u_X	Uncertainty in gas X (molmol^{-1})
V_{contam}/V	Fraction of contamination ($\mathrm{m}^3\mathrm{m}^{-3}$)
w_{air}	Downward velocity of air (ms^{-1})
w_{ice}	Downward velocity of ice layers (ms^{-1})
$[X]$	Mixing ratio of gas X (molmol^{-1})
x_{air}	Air content of ice (mL STP per kg ice)
z	Depth (m)
z_{COD}	Full close-off depth; $s_{\text{op}}(z_{\text{COD}}) = 0$ (m)
z_{LID}	Lock-in depth (m)
γ_X	Diffusion coefficient relative to CO_2
Δage	Ice age-gas age difference (yr)
$\Delta\text{age}_{\text{op}}$	Ice age- open pore gas age difference (yr)
ΔM	Molar mass deviation from air (kgmol^{-1})
Δt	Temporal step size (s) or (yr)
Δz	Spatial step size (m)
δ_{grav}	Gravitational fractionation p. unit mass (‰)
Θ	Temperature (° C)
μ	Mean value of a series
ρ	Firn density (gcm^{-3})
ρ_{co}	Mean close-off density (gcm^{-3})
ρ_{COD}	Full close-off density; $\rho(z_{\text{COD}})$ (gcm^{-3})
ρ_{ice}	Solid ice density (gcm^{-3})
σ_i	Assigned uncertainty for data point i
τ	Tortuosity
τ_0	Initial guess for τ in tuning algorithm

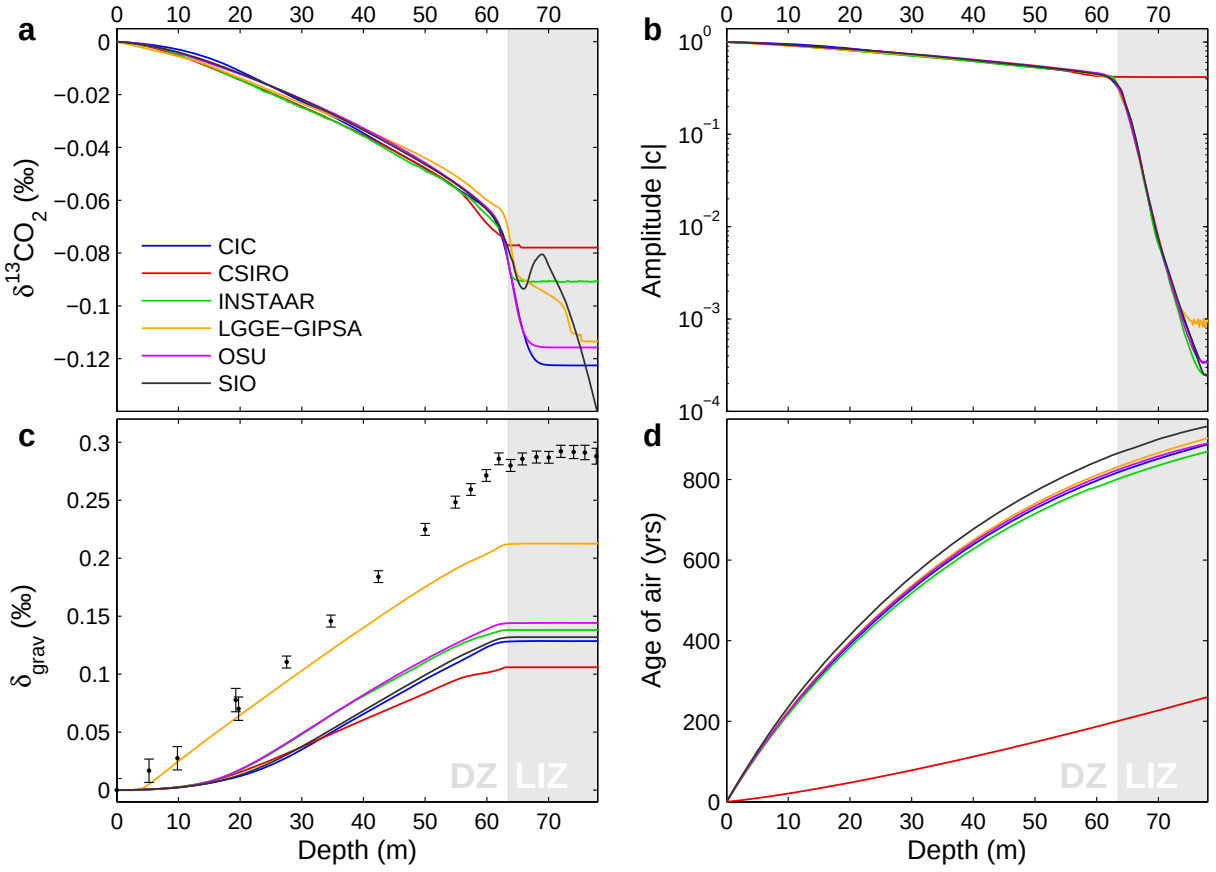

Fig. 8. Model comparison using the four diagnostic scenarios and diffusivity tuned to the US borehole data. **(a)** Scenario I: Diffusive fractionation for a hypothetical monotonic CO2 increase. **(b)** Scenario II: Attenuation of a 15 yr period sinusoidal CO_2 forcing with depth. **(c)** Scenario III: Gravitational enrichment for gas X with $D^0_X = 0.025 D^0_{CO2}$. Data points show gravitational enrichment of $^{15}N_2$ corrected for the effect of thermal diffusion. **(d)** Scenario IV: Mean age of gas Y, using advective transport only ($D^0_Y = 0$). With the exception of S-III all scenarios were run with the effect of gravity turned off.

Table 8. Details on running the diagnostic scenarios.

Gas	Mass ($g\,mol^{-1}$)	D/D_{CO_2}	Scenario file	Gravity	Run time (yr CE)
			Scenario I		
$^{12}CO_2$	43.99	1.000048	Diagnostic_1.txt	OFF	1800-2008.54
$^{13}CO_2$	44.99	0.995613	Diagnostic_1.txt	OFF	1800-2008.54
			Scenario II		
CO_2	44.01	1	Diagnostic_2a.txt	OFF	1800-2008.54
CO_2	44.01	1	Diagnostic_2b.txt	OFF	1800-2008.54
			Scenario III		
X	M_{air}+1	0.025	Diagnostic_3.txt	ON	1000-2008.54
			Scenario IV		
Y	44.01	0	Diagnostic_4.txt	OFF	400-2008.54

References

Buizert, C.: The influence of firn air transport processes and radiocarbon production on gas records from polar firn and ice, Ph.D. thesis, 2012.

Chen, N. H. and Othmer, D. F.: New Generalized Equation for Gas Diffusion Coefficient, J. Chem. Eng. Data, 7, 37–41, 1962.

Etheridge, D., Steele, L., Francey, R., and Langenfelds, R.: Atmospheric methane between 1000 AD and present: Evidence of anthropogenic emissions and climatic variability, J. Geophys. Res.-Atm., 103, 15 979–15 993, 1998.

Etheridge, D. M., Steele, L. P., Langenfelds, R. L., Francey, R. J., Barnola, J. M., and Morgan, V. I.: Natural and anthropogenic changes in atmospheric CO_2 over the last 1000 years from air in Antarctic ice and firn, J. Geophys. Res., 101, 4115–4128, 1996.

Francey, R., Allison, C., Etheridge, D., Trudinger, C., Enting, I., Leuenberger, M., Langenfelds, R., Michel, E., and Steele, L.: A 1000-year high precision record of delta C-13 in atmospheric CO_2, Tellus B, 51, 170–193, 1999.

Haupt, R. L. and Haupt, S. E.: Practical Genetic Algorithms, John Wiley & Sons, Inc., Hoboken, New Jersey, 1998.

Karlen, I., Olsson, I. U., Kallburg, P., and Kilici, S.: Absolute determination of the activity of two ^{14}C dating standards, Arkiv Geofysik, 4, 465–471, 1968.

Kawamura, K., Severinghaus, J. P., Ishidoya, S., Sugawara, S., Hashida, G., Motoyama, H., Fujii, Y., Aoki, S., and Nakazawa, T.: Convective mixing of air in firn at four polar sites, Earth Planet Sc. Lett., 244, 672–682, 2006.

Levin, I. and Kromer, B.: The tropospheric (CO_2)-C-14 level in mid-latitudes of the Northern Hemisphere (1959-2003), Radiocarbon, 46, 1261–1272, 2004.

Levin, I., Hammer, S., Kromer, B., and Meinhardt, F.: Radiocarbon observations in atmospheric CO_2: Determining fossil fuel CO_2 over Europe using Jungfraujoch observations as background, Sci. Total Environ., 391, 211–216, 2008.

Manning, M. and Melhuish, W. H.: Atmospheric Delta 14C record from Wellington, in: Trends: A Compendium of Data on Global Change, Carbon Dioxide Information Analysis Center, Oak Ridge National Laboratory, U.S. Department of Energy, Oak Ridge, Tenn., U.S.A., 1994.

Martinerie, P., Nourtier-Mazauric, E., Barnola, J. M., Sturges, W. T., Worton, D. R., Atlas, E., Gohar, L. K., Shine, K. P., and Brasseur, G. P.: Long-lived halocarbon trends and budgets from atmospheric chemistry modelling constrained with measurements in polar firn, Atmos. Chem. Phys., 9, 3911–3934, 2009.

Matsunaga, N., Hori, M., and Nagashima, A.: Diffusion coefficients of global warming gases into air and its component gases, High Temp.-High Press., 30, 77–83, 1998.

Matsunaga, N., Hori, M., and Nagashima, A.: Measurements of the mutual diffusion coefficients of gases by the Taylor method (7th Report, measurements on the SF_6-air, SF_6-N_2, SF_6-O_2, CFC12-N_2, CFC12-O_2, HCFC22-N_2 and HCFC22-O_2 systems), Trans. Jpn. Soc. Mech. Eng. B., 68, 550–555, 2002a.

Matsunaga, N., Hori, M., and Nagashima, A.: Measurements of the mutual diffusion coefficients of gases by the Taylor method (8th Report, measurements on the HFC32-air, HCFC124-air, HCFC125-air, HCFC143a-air, and HFC43-10mee-air systems), Trans. Jpn. Soc. Mech. Eng. B., 68, 550–555, 2002b.

Matsunaga, N., Hori, M., and Nagashima, A.: Measurements of the mutual diffusion coefficients of carbon tetrafluoride and methyl bromide into air, nitrogen and oxygen, Proc 26th Jpn Symp Therm Props, 26, 499–501, 2005.

Matsunaga, N., Hori, M., and Nagashima, A.: Gaseous diffusion coefficients of dimethyl ether and diethyl ether into air, nitrogen and oxygen, Netsu Bussei, 20, 83–86, 2006.

Matsunaga, N., Hori, M., and Nagashima, A.: Gaseous diffusion coefficients of propane and propylene into air, nitrogen and oxygen, Netsu Bussei, 20, 83–86, 2007.

Matsunaga, N., Hori, M., and Nagashima, A.: Gaseous diffusion coefficients of methyl bromide and methyl iodide into air, nitrogen and oxygen, Heat Trans. Asian Res., 38, doi:10.1002/htj.20255, 2009.

Nydal, R. and Lövseth, K.: Carbon-14 Measurements in Atmospheric CO_2 from Northern and Southern Hemisphere Sites, 1962-1993, Carbon Dioxide Information Analysis Center, Oak Ridge National Laboratory, Oak Ridge, Tennessee, 1996.

Reimer, P., Baillie, M., Bard, E., Bayliss, A., Beck, J., Bertrand, C., Blackwell, P., Buck, C., Burr, G., Cutler, K., Damon, P., Edwards, R., Fairbanks, R., Friedrich, M., Guilderson, T., Hogg, A., Hughen, K., Kromer, B., McCormac, G., Manning, S., Ramsey, C., Reimer, R., Remmele, S., Southon, J., Stuiver, M., Talamo, S., Taylor, F., van der Plicht, J., and Weyhenmeyer, C.: IntCal04 terrestrial radiocarbon age calibration, 0-26 cal kyr BP, Radiocarbon, 46, 1029–1058, 2004.

Rommelaere, V., Arnaud, L., and Barnola, J. M.: Reconstructing recent atmospheric trace gas concentrations from polar firn and bubbly ice data by inverse methods, J. Geophys. Res.-Atm, 102, 30 069–30 083, 1997.

Schwander, J., Barnola, J. M., Andrie, C., Leuenberger, M., Ludin, A., Raynaud, D., and Stauffer, B.: The age of the air in the firn and the ice at Summit, Greenland, J. Geophys. Res.-Atm, 98, 2831–2838, 1993.

Severinghaus, J. P. and Battle, M. O.: Fractionation of gases in polar lee during bubble close-off: New constraints from firn air Ne, Kr and Xe observations, Earth Planet Sc. Lett., 244, 474–500, 2006.

Severinghaus, J. P., Grachev, A., and Battle, M.: Thermal fractionation of air in polar firn by seasonal temperature gradients, Geochem. Geophy. Geosy., 2, 2001.

Severinghaus, J. P., Albert, M. R., Courville, Z. R., Fahnestock, M. A., Kawamura, K., Montzka, S. A., Muhle, J., Scambos, T. A., Shields, E., Shuman, C. A., Suwa, M., Tans, P., and Weiss, R. F.: Deep air convection in the firn at a zero-accumulation site, central Antarctica, Earth Planet Sc. Lett., 293, 359–367, 2010.

Trudinger, C. M., Enting, I. G., Etheridge, D. M., Francey, R. J., Levchenko, V. A., Steele, L. P., Raynaud, D., and Arnaud, L.: Modeling air movement and bubble trapping in firn, J. Geophys. Res.-Atm, 102, 6747–6763, 1997.

Witrant, E., Martinerie, P., Hogan, C., Laube, J. C., Kawamura, K., Capron, E., Montzka, S. A., Dlugokencky, E. J., Etheridge, D., Blunier, T., and Sturges, W. T.: A new multi-gas constrained model of trace gas non-homogeneous transport in firn: evaluation and behavior at eleven polar sites, Atmos. Chem. Phys. Discuss., 11, 23 029–23 080, doi:10.5194/acpd-11-23029-2011, 2011.

WMO: Scientific Assessment of Ozone Depletion: 2006. Global Ozone Research and Monitoring Project - Report No.50, World Meteorological Organization, Geneva, http://ozone.unep.org/Publications, 2007.